AGU ADVANCING EARTH AND SPACE SCIENCES

JGR Solid Earth

RESEARCH ARTICLE
10.1029/2026JB033859

Distinct Groundwater Regimes in West Antarctic Sedimentary Basins Inferred From Magnetotelluric Imaging

Siobhan F. Killingbeck[1], Bernd Kulessa[1,2], Rebecca Pearce[3], Alex Brisbourne[4], Louise Borthwick[5], Felipe Napoleoni[6], Sridhar Anandakrishnan[7], Martyn Unsworth[8], and Atsuhiro Muto[5]

[1]Department of Geography, Faculty of Science and Engineering, Swansea University, Swansea, UK, [2]School of Natural Sciences (Physics), University of Tasmania, Dynnyrne, TAS, Australia, [3]Cascade Institute, Royal Roads University, Victoria, BC, Canada, [4]British Antarctic Survey, Cambridge, UK, [5]Earth and Environmental Science, Temple University, Philadelphia, PA, USA, [6]School of Geosciences, University of Edinburgh, Edinburgh, UK, [7]Department of Geosciences, Pennsylvania State University, University Park, PA, USA, [8]Department of Physics, Faculty of Science, University of Alberta, Edmonton, AB, Canada

Key Points:

- The electrical properties of Thwaites Glacier subglacial basin are derived from new magnetotelluric data
- Subglacial electrical properties at Thwaites Glacier basin are evaluated against legacy West Antarctic and South Pole magnetotelluric data
- Varied, spatially complex groundwater regimes are suggested from distinct basin properties across West Antarctica

Supporting Information:

Supporting Information may be found in the online version of this article.

Correspondence to:

S. F. Killingbeck,
s.f.killingbeck@swansea.ac.uk

Citation:

Killingbeck, S. F., Kulessa, B., Pearce, R., Brisbourne, A., Borthwick, L., Napoleoni, F., et al. (2026). Distinct groundwater regimes in west Antarctic sedimentary basins inferred from magnetotelluric imaging. *Journal of Geophysical Research: Solid Earth*, *131*, e2026JB033859. https://doi.org/10.1029/2026JB033859

Received 22 JAN 2026
Accepted 22 AUG 2026

Author Contributions:

Conceptualization: Bernd Kulessa
Data curation: Siobhan F. Killingbeck, Rebecca Pearce
Formal analysis: Siobhan F. Killingbeck, Rebecca Pearce, Martyn Unsworth
Funding acquisition: Bernd Kulessa, Alex Brisbourne, Sridhar Anandakrishnan
Investigation: Rebecca Pearce, Alex Brisbourne, Louise Borthwick, Felipe Napoleoni, Sridhar Anandakrishnan
Methodology: Siobhan F. Killingbeck, Bernd Kulessa
Project administration: Bernd Kulessa, Alex Brisbourne, Sridhar Anandakrishnan

Abstract Subglacial sedimentary basins in Antarctica are hypothesized to modulate ice flow and biogeochemical cycles via groundwater and geothermal feedbacks, yet their properties remain poorly constrained. Here, we present a joint quantitative analysis of new magnetotelluric (MT) data acquired at Thwaites Glacier (TG) and WAIS Divide, alongside legacy data sets from Whillans Ice Stream, Ross Ice Shelf, and South Pole. The new MT data reveal a shallow 1-D crustal structure, around the ice bed interface, at TG, overlying deeper 3-D structures. Our constrained 1-D transdimensional Bayesian inversion of the upper crust highlights that the sedimentary basin beneath TG exhibits relatively high resistivity (>10 Ωm), distinct from the lower-resistivity (<10 Ωm) basins at other sites. Sensitivity analysis reveals that the TG basin is horizontally heterogeneous, with conductive signatures in thicker sections and resistive signatures at GHOST Ridge, a subglacial topographic high which has been identified as a potential future stabilizing point. Conversely, basins beneath Subglacial Lake Whillans and the South Pole exhibit vertical stratification, with relatively resistive upper layers, up to 600 m thick, above conductive deeper layers (<5 Ωm). We hypothesize that complex, spatially variable groundwater regimes are widespread in Antarctica. These contrasting hydrological environments imply continent-scale variability in subglacial thermodynamics and possible modulation of inherent ice dynamics.

Plain Language Summary Beneath the massive ice sheets of Antarctica lie deep sedimentary basins holding vast groundwater. This water acts as a lubricant, controlling how fast the ice flows into the ocean, while also influencing how chemicals and carbon are stored and released into the sea. Despite its importance, these deep systems remain poorly understood. Here, we used a deep-earth imaging technique to characterize the groundwater systems beneath key sites, including the fast-flowing Thwaites Glacier. Our results show that these groundwater systems are not the same across the continent. Basins beneath Thwaites Glacier potentially have different properties compared to other areas, especially at GHOST Ridge, a topographic high that may help stabilize Thwaites Glacier in the future. In contrast, other sites like Whillans Ice Stream and the South Pole have layers within their groundwater systems. These findings show that groundwater under Antarctica is diverse.

1. Introduction

Sedimentary basins are widespread geological features in Antarctica, and facilitate dynamic feedbacks with the potential to drive rapid ice-sheet change (Aitken et al., 2023; Li et al., 2022). However, in situ observations of these basins remain sparse, and their properties and inherent processes affecting ice-sheet hydrology and flow, remain poorly understood due to the challenges of surveying vast, kilometer thick (Morlighem et al., 2020), ice-covered regions (Aitken et al., 2023; Cox et al., 2023). Critically, these basins can contain extensive groundwater reservoirs which supply water to the ice-bed interface (Siegert et al., 2018), acting as a lubricant for fast ice flow (Figure 1a), a process that can be amplified by ice-sheet retreat (Li et al., 2022). Sedimentary basins also provide a source of easily erodible material, forming a deformable bed of subglacial till that further enhances sliding of the overlying ice sheet (Alley et al., 1987; Anandakrishnan et al., 1998). Where upward groundwater flow occurs from depth, it can advect geothermal heat to the ice-bed interface, leading to basal melting and creating a positive

Resources: Siobhan F. Killingbeck, Bernd Kulessa, Martyn Unsworth
Software: Siobhan F. Killingbeck, Martyn Unsworth
Supervision: Bernd Kulessa, Martyn Unsworth
Validation: Siobhan F. Killingbeck
Visualization: Siobhan F. Killingbeck, Felipe Napoleoni
Writing – original draft: Siobhan F. Killingbeck, Bernd Kulessa
Writing – review & editing: Siobhan F. Killingbeck, Bernd Kulessa, Rebecca Pearce, Alex Brisbourne, Martyn Unsworth, Atsuhiro Muto

feedback loop (Gooch et al., 2016). Furthermore, the basin topography (Figure 1b) and ice surface slope can dictate the routing of subglacial water, potentially diverting it from its current ice catchment (e.g., Napoleoni et al., 2020) and linking otherwise separate catchments, propagating ice-sheet instability across the continent (Alley et al., 1994). Finally, these basins may function as critical components of the Antarctic biogeochemical cycle, serving as reservoirs for sequestered organic carbon. The specific groundwater regime, defined by salinity and residence time, controls the mobilization of this carbon and its eventual discharge as dissolved nutrients into the Southern Ocean (Mikucki et al., 2015).

Geologically, subglacial sedimentary basins have very different characteristics in different parts of the Antarctic continent (Figure 1c). West Antarctic basins are typically the result of subsidence caused by crustal extension of the West Antarctic Rift System (WARS). In contrast, basins beneath the East Antarctic Ice Sheet (EAIS), such as the South Pole Basin, are more commonly related to the older, more stable cratonic shield (Figure 1c; Aitken et al., 2023).

Around 80% of the West Antarctic Ice Sheet (WAIS) is grounded below sea level, making it highly susceptible to a self-perpetuating process known as the marine ice-sheet instability (MISI) (Schoof, 2012; Weertman, 1974). MISI is a positive feedback loop where the grounding line retreats onto a bed that deepens inland and increases ice flux, accelerates ice flow and drives further, potentially irreversible, retreat. Most of the WAIS sits on the extended, subsided crust of the WARS, a major tectonic feature with a well-defined boundary at the Transantarctic Mountains (Figure 1b; Jordan et al., 2020). Many of West Antarctica's fast-flowing glaciers and ice streams (Figure 1a), such as those along the Siple Coast (Anandakrishnan et al., 1998; Bell et al., 1998; Peters et al., 2006) and the Ferrigno Ice Stream (Bingham et al., 2012), flow along rift-formed, fault-bounded sedimentary basins characterized by smooth beds. However, in contrast, the Thwaites Glacier (TG) flows across a series of ridges and troughs and is unconfined by structures formed by rifting (Borthwick et al., 2025; Jordan et al., 2023).

The WAIS is currently losing ice mass at an accelerating rate, with the glaciers in the Amundsen Sea Embayment being the primary agents of this loss (Mouginot et al., 2014). Of these, TG is the most likely location that could lead to the collapse of the WAIS (Scambos et al., 2017), due to its large ice drainage basin and inland-deepening bed which makes it highly susceptible to MISI. However, the timing and magnitude of this retreat are highly uncertain and not reproduced consistently by ice-sheet models, mainly due to a lack of detailed information about the subglacial boundary conditions (Schwans et al., 2023).

Dense, targeted airborne geophysical surveys have facilitated the generation of a geological map of the crust beneath the TG (e.g., Jordan et al., 2023). Bed properties were derived from recent seismic surveys (Clyne et al., 2020; Muto et al., 2019) and have been directly incorporated into ice-dynamic models, demonstrating that a mixed bed produces faster retreat compared to models assuming either an entirely hard or a soft bed (Schwans, 2026). However, Antarctic subglacial hydrological models and ice-dynamic models only consider the shallow hydrologic systems and properties directly at the ice-bed interface (e.g., Schwans et al., 2023), not least because commonly used geophysical techniques (e.g., radar, active and passive seismics, gravity, and magnetics do not provide direct constraints on deep groundwater properties or connectivity between the shallow and deep hydrologic systems (e.g., Bell et al., 1998). The magnetotelluric (MT) method holds promise in addressing these challenges (e.g., Gustafson et al., 2022).

The MT method is commonly used in terrestrial settings for geothermal energy exploration and mapping subsurface fluids (e.g., García & Díaz, 2016; Samrock et al., 2015; Unsworth & Rondenay, 2013). MT measures subsurface bulk electrical resistivity, the inverse of conductivity, which is highly sensitive to lithology, temperature, and the presence of aqueous fluids. Generally, resistivity decreases as salinity, effective porosity, and temperature increase. This sensitivity is largely driven by pore fluid composition: freshwater is relatively resistive (20–200 Ωm), brackish water and seawater are conductive (0.2–20 Ωm), and brines are highly conductive (<0.2 Ωm) (Lewis & Perkin, 1981). Consequently, MT is a valuable technique for investigating the subglacial environment, particularly in regions characterized by variations in lithology, geothermal heat flow (GHF), and saline groundwater within sedimentary basins (e.g., Gustafson et al., 2022; Key & Siegfried, 2017; Killingbeck et al., 2022; Kulessa et al., 2019; Mikucki et al., 2015).

Despite its proven utility, the application of MT in Antarctica remains sparse (Hill, 2020). Existing West Antarctic data sets are limited to profiles on the Whillans Ice Stream (44 stations; Gustafson et al., 2022), Central

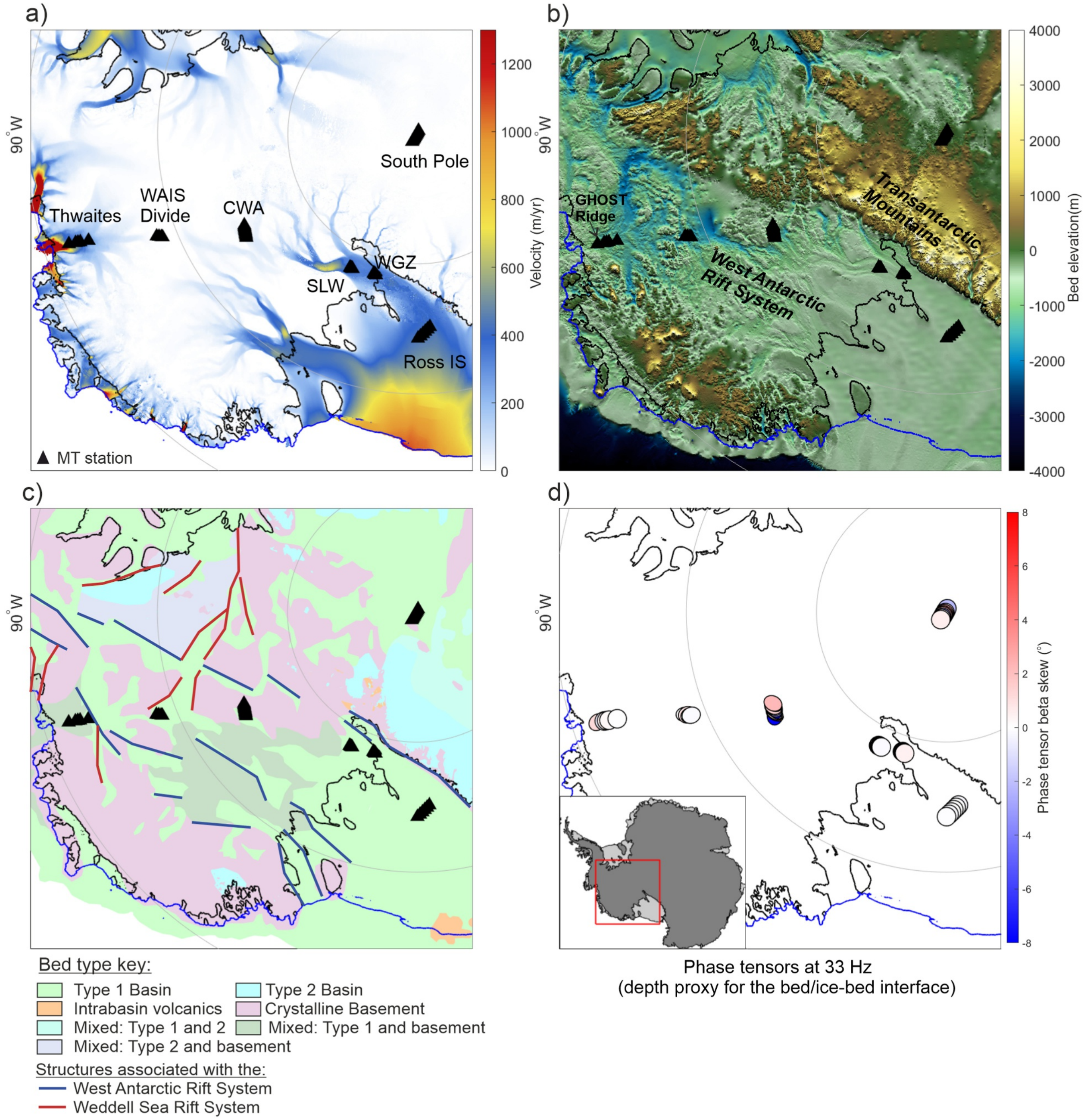

Figure 1. (a) West Antarctic ice flow speeds from MEaSUREs InSAR Phase-Based Antarctica Ice Velocity Map (Mouginot et al., 2019) with new, Thwaites and WAIS Divide, and legacy, Central West Antarctica (CWA), South Pole, Subglacial Lake Whillans (SLW), Whillans grounding zone (WGZ) and Ross Ice Shelf (IS), MT survey locations. (b) Bed elevation from BedMachine Antarctica V3 (Morlighem et al., 2020). All elevations are referred to as the WGS84 ellipsoid. (c) Classification of geological bed types and structures in West Antarctica (Aitken et al., 2023). (d) The MT phase-tensors (Caldwell et al., 2004) at 33 Hz, a depth proxy for the bed/ice-bed interface. This figure was created using the Antarctic Mapping Tools (Greene et al., 2017).

West Antarctica (10 stations; Wannamaker et al., 1996), and the Ross Ice Shelf (where 57 stations were acquired across the Transantarctic Mountains; Wannamaker et al., 2017) (Figure 1). Additionally, in East Antarctica, MT stations have been acquired over the South Pole sedimentary basin (10 stations; Wannamaker et al., 2004) (Figure 1). To address this data gap, we acquired new MT data at the WAIS Divide (4 stations) and Thwaites Glacier (TG) (5 stations) during the austral summers of 2022/2023 and 2023/2024 as part of the International Thwaites Glacier Collaboration's GHOST project (Figure 1). Here, we present a joint quantitative analysis of these data sets to provide new insights into Antarctic sedimentary basins and crustal structures. Using a constrained 1-D trans-dimensional Bayesian inversion, we produced depth-resistivity models for the uppermost crust beneath the ice-bed interface, allowing for the interpretation of the geological, geothermal, and hydrogeological properties of the underlying sedimentary basins.

2. Material and Methods

In the austral summer of 2022–2023, we acquired four MT stations at WAIS Divide, where the ice flow is slow (<10 m yr^{-1}; Figure 1a) and no sedimentary basins are thought to be present (Figure 2a; Jordan et al., 2023). In the austral summer of 2023–24, five MT stations were acquired on TG where the ice flow is relatively fast (300 m yr^{-1} to 500 m yr^{-1}; Figure 1a) and subglacial sedimentary basins have been delineated by Jordan et al. (2023) and Borthwick et al. (2025) (Figure 2a). These 9 MT stations were the only stations deployed; the deployment of additional MT stations, including a remote reference station, was planned but ultimately precluded by logistical challenges and adverse weather conditions. At TG, the farthest downstream station was located on the GHOST Ridge, a subglacial topographic high (Figure 2a; Borthwick et al., 2025), which has been identified as a potential future stabilizing point (e.g., Schwans et al., 2023), 70 km inland of the current grounding zone. The other four MT stations were located up to 80 km upstream of GHOST Ridge (Figure 2a).

We used the Phoenix Geophysics Ultra-Wideband Magnetotelluric (UMT) system, consisting of a five-channel UMT receiver (MTU-5C), three MTC-150/155 induction sensors and perforated titanium plate electrodes and preamplifiers. A 100Ah battery, supplied by a 50W solar panel on a Morningstar 10A regulator, was used to power the stations. The station on GHOST Ridge (53° declination) and 4 stations at WAIS Divide (62° declination) were deployed in a local geomagnetic co-ordinate system and measurements were rotated mathematically to a co-ordinate system aligned with true, geographic, north, to ensure a consistent reference frame. The other 4 stations acquired on TG were deployed in a coordinate system aligned with true north. Perpendicular electric field dipoles were installed with ∼100 m separation between electrodes. The sheet electrodes were buried in the snow, and preamplifiers connected to each dipole electrode. A perforated titanium sheet was also used as the ground electrode of each station. Magnetic field components were measured using three induction coils oriented in the X (North), Y (East) and Z (vertically downwards) directions. A low-pass filter of 10 kHz was applied to the time-series data primarily as anti-aliasing filter. Data were recorded continuously at 150 Hz, supplemented by periodic 24 kHz high-frequency bursts lasting 1 s every 60 s.

The raw time-series data were processed using the Phoenix Geophysics EMpower software to produce estimates of apparent resistivity and phase in the frequency range of ∼200–0.001 Hz (Table S1, Figures S1–S9 in Supporting Information S1). Higher frequencies (>200 Hz) were removed because the apparent resistivity curves exhibit a sharp, unphysical decrease. This effect is attributed to an unintended RC low-pass filter formed by the extreme contact resistance of the snow/firn layer likely interacting with the internal input capacitance of the preamplifiers and/or cables.

Data quality was variable across the measured stations. In general, the data collected at WAIS Divide were less noisy than those from TG, a difference that can be primarily attributed to windier conditions at TG. Furthermore, several stations in both regions experienced data degradation in the natural source deadband frequency range, centered around 1 Hz (Chave & Jones, 2012), rendering these specific data points unusable (Figure 2; Figures S1–S9 in Supporting Information S1). For apparent resistivity, depth of investigation increases as frequency decreases, with XY calculated from the X-component of the electric field and the Y-component of the magnetic field. YX is calculated from the Y-component of the electric field and the X-component of the magnetic field.

The dimensionality of the MT data was investigated using the phase tensor approach (Caldwell et al., 2004). This gives a graphical representation of the azimuthal variation of the MT impedances and shows if the data can be considered 1-D, 2-D or 3-D. The phase tensors principal value can provide relevant information on electrical resistivity gradients and their variation with depth. Furthermore, the phase-tensor geoelectric strike direction gives an indication of the orientation of the crustal electrical resistivity structure (Figures 1d and 2a; Figure S10 in Supporting Information S1). Real induction vectors were also calculated from the tipper data and plotted using the Parkinson convention (Parkinson, 1959), where vectors point toward regions of low resistivity (i.e., enhanced conductivity) (Figures S11 and S12 in Supporting Information S1). These vectors reflect lateral conductivity gradients and can locate the position of conductive anomalies relative to the station, aiding in the differentiation between the location of the conductor and the geoelectric strike defined by the phase tensors.

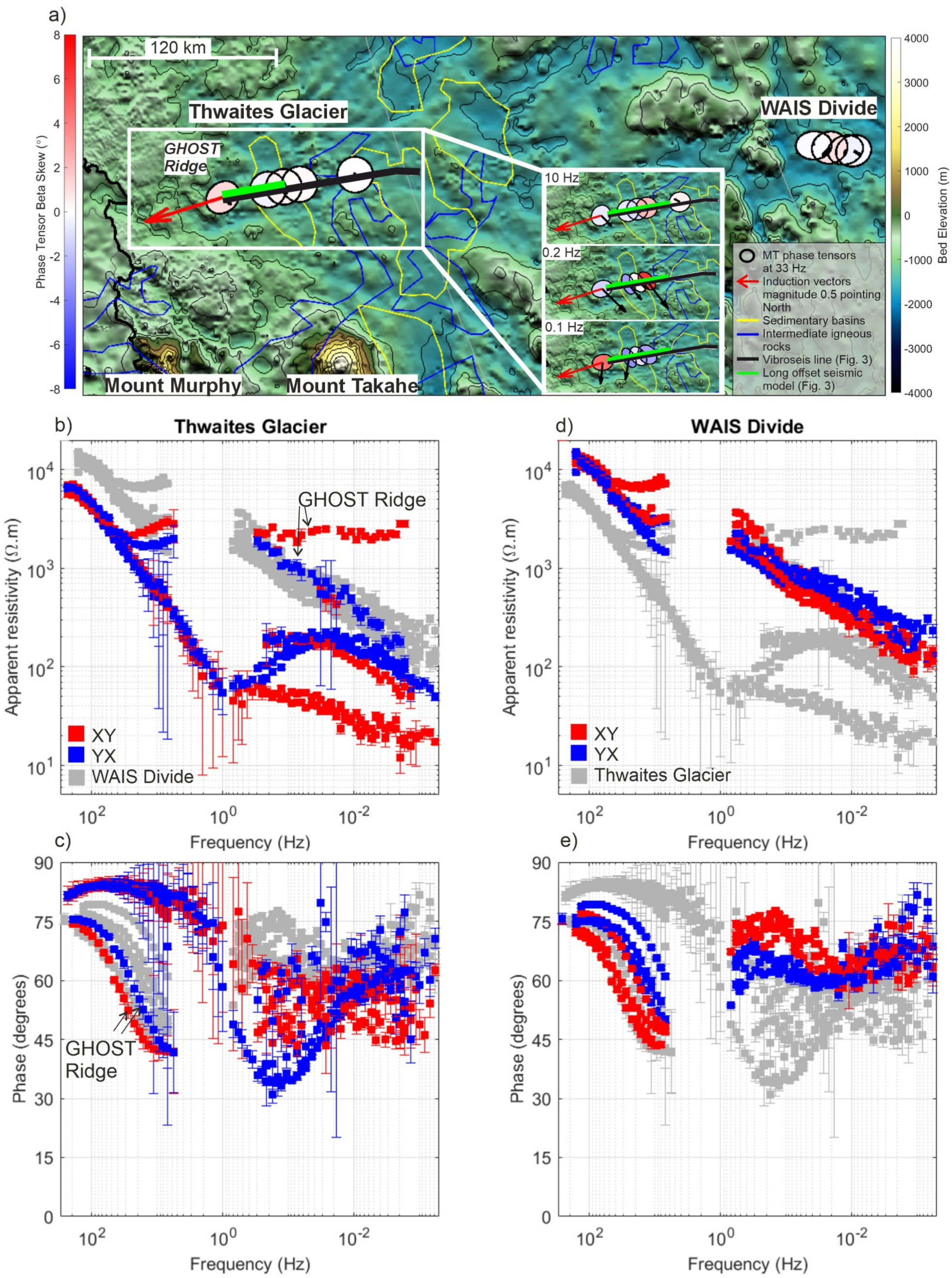

Figure 2. (a) Thwaites Glacier and WAIS Divide bed elevation from BedMachine Antarctica V3 (Morlighem et al., 2020), MT phase tensor and real induction vectors, plotted using the Parkinson convention (Parkinson, 1959), at a frequency of 33 Hz. Additionally, 10, 0.2, and 0.1 Hz are plotted at TG. The geological outlines are from Jordan et al. (2023). The scale factor applied to the ellipse size of the phase tensors is 0.1°, and the scale factor applied to the tipper magnitude is 100 km per unit, that is, a magnitude 1 arrow is 100 km long. A reference induction vector is plotted in red with magnitude 0.5 and is pointing North from TG7, GHOST Ridge. All elevations are referred to as the WGS84 ellipsoid. (b) Apparent resistivity and (c) phase for the MT data acquired on Thwaites Glacier with WAIS Divide data plotted in the background in gray, (d) apparent resistivity and (e) phase for the MT data acquired at WAIS Divide with Thwaites Glacier data plotted in the background in gray.

To visualize the approximate penetration depth of the MT signals, we calculated the real part of the complex Schmucker-Weidelt *C*-response (z^*), which acts as a frequency-dependent proxy for the depth of the induced telluric currents (Schmucker, 1970; Weidelt, 1972). We extracted the ice thickness at each station from

10.1029/2026JB033859

BedMachine v3 (Morlighem et al., 2020) and plotted it alongside our depth proxy (Figure S13 in Supporting Information S1). The depth proxy indicates that the MT signals penetrate to approximately 5–6 km at the WAIS Divide and Ghost Ridge sites, and to ∼3 km at the remaining TG stations, before encountering the deadband frequencies.

Given the sparse MT station coverage and the similarity between the XY and YX curves in our depth proxy plot at the ice-bed interface and for the upper ∼5 km (Figure S13 in Supporting Information S1), we selected a 1-D modeling approach, as this provides the most practical and well-constrained interpretation. We therefore employed a constrained 1-D trans-dimensional Bayesian inversion method, MuLTI-MT (Killingbeck, 2025), to model the crustal resistivity structure. To implement this process, a data quantity that is rotationally invariant, the sum of squared elements of the impedance tensor, Z_{ssq}, was used (Equation 1; Rung-Arunwan et al., 2017).

$$Z_{\mathrm{ssq}} = \sqrt{(Z_{\mathrm{xx}}^2 + Z_{\mathrm{xy}}^2 + Z_{\mathrm{yx}}^2 + Z_{\mathrm{yy}}^2)/2} \tag{1}$$

This quantity is mathematically invariant regarding the coordinate system rotation and yields an orientation-independent model that is bounded by the results from the individual Z_{xy} and Z_{yx} components. We also independently inverted the Z_{xy} and Z_{yx} impedance tensors to validate of the Z_{ssq} inversion, and to identify at which depths the resulting resistivity models diverge, thereby highlighting the limitations of our 1-D inversion approach. The Bayesian Z_{ssq} inversion is trans-dimensional in that it determines the number of subsurface layers from the data. The method also features a robust uncertainty assessment to reliably quantify the subglacial bulk resistivity and explore the entire model space.

The inversion for each station was constrained by ice-thickness data from BedMachine v3 (Morlighem et al., 2020), with resistivity bounds set to 5,000−100,000 Ωm for the ice layer (Killingbeck et al., 2024; Kulessa, 2007). Below the ice, the permitted resistivity range was broadened to 0.1−1,000,000 Ωm. Additionally, at TG the thickness of the sedimentary basins was constrained by the results from the long offset seismic data and vibroseis data acquired as part of the ITGC GHOST project, respectively reported in Borthwick et al. (2025) and Zeising et al. (2026) (Figure 2a). Here, the resistivity bounds within the sedimentary basin were set to 0.1−1,000 Ωm. This range was chosen to encompass all plausible values for a subglacial sedimentary basin, from units saturated with highly conductive brines (∼0.1 Ωm) to more compacted, resistive sediments (<1,000 Ωm). A 5% relative error floor was imposed on the impedance tensor components to establish the minimum data uncertainty, defining the level of acceptable misfit in the Bayesian framework. This value prevents the inversion from fitting noise and facilitates efficient exploration of the model space, ensuring the resulting models are meaningfully constrained by the data. All inversion parameters, including frequency ranges used in each inversion, are detailed in Table S1 of Supporting Information S1. To provide a comparative assessment, we also applied a 1-D Occam's inversion (Constable et al., 1987) to the same data sets (Table S2 in Supporting Information S1). This approach, which seeks the smoothest possible resistivity model that fits the MT data, serves as a crucial validation step for our primary Bayesian inversion results. While our Bayesian inversion provides a comprehensive probabilistic assessment of resistivity model parameters, the Occam's inversion offers an alternative perspective by generating a smooth model that adequately fits the observed MT data. The consistent recovery of key features across both inversion types demonstrates that our interpretations are not artifacts of a single inversion algorithm.

At each station, we identified the bulk median (50% credible interval) subglacial resistivity by creating a histogram of values from the posterior distribution of the Bayesian inversions for the material beneath the ice sheet. If the median resistivity was less than 200 Ωm, the lithology was interpreted as being consistent with sedimentary basin material. A resistivity threshold of 200 Ωm is a reasonable value to delineate sedimentary basins, as it effectively accounts for a wide range of basin properties (Telford et al., 1990). While many sedimentary basins exhibit low-resistivity values, often below 100 Ωm (e.g., Gustafson et al., 2022), factors such as low porosity, the presence of freshwater or hydrocarbons, or low temperatures can result in higher resistivity. Crucially, this value remains significantly lower than the resistivity of both crystalline bedrock (typically >1,000 Ωm; Mikucki et al., 2015) and glacial ice (typically >10,000 Ωm; Kulessa, 2007; Mikucki et al., 2015; Killingbeck et al., 2024), ensuring a clear distinction between these geological units. If the median resistivity of the subglacial material was greater than 200 Ωm, we interpreted this as metasedimentary rocks or bedrock. For locations with an interpreted subglacial sedimentary basin, we defined the basin's base as the depth where the upper bound of the 68% resistivity credible interval (one standard deviation) first exceeds 200 Ωm. The basin's thickness was then calculated by subtracting the ice thickness from the BedMachine v3 data set (Morlighem et al., 2020). We define this thickness as the minimum sedimentary basin thickness required to fit the observed data at each MT station.

To validate our methodology and its ability to resolve basin parameters, we created two synthetic 1-D resistivity models. The first model consisted of 2.5 km of ice above a 5 km thick sedimentary basin (50 Ωm) and a resistive bedrock (5,000 Ωm). The second model comprised 2.5 km of ice above a 1 km thick sedimentary basin (10 Ωm), again overlying 5,000 Ωm bedrock. The sedimentary basins in both models were designed to have an identical conductance of 100 S (the product of thickness and conductivity). It is well known that MT can determine the conductance of a low-resistivity layer, but not the individual values of thickness and conductivity. In this study, this limitation was overcome because the resistivity of the ice layer is well constrained. Our results show that the inversion methodology accurately recovers the true model parameters for both scenarios to within one standard deviation (Figure S14 in Supporting Information S1).

3. Results

3.1. New MT Surveys at Thwaites Glacier and WAIS Divide

At WAIS Divide, both XY and YX apparent resistivity indicate relatively high bulk electrical resistivity at frequencies of 160–1 Hz (Figure 2d), corresponding to depths in the range 0–6 km (Figure S13 in Supporting Information S1), which is consistent with the absence of a sedimentary basin. The similarity of the XY and YX apparent resistivity spanning the ice-bed interface (Figure S13 in Supporting Information S1) indicates a likely 1-D shallow resistivity structure (Figure S13 in Supporting Information S1). This is confirmed by the phase tensors that plot with a near circular shape and exhibit low skew values at the highest frequencies (∼160–10 Hz; Figure S10b in Supporting Information S1). Below a frequency of 1 Hz, the XY and YX apparent resistivity curves begin to separate, and the phase tensors show an East-West orientation of the major axes (between 1 and 0.1 Hz) that rotates toward a Northwest-Southeast orientation at lower frequencies (<0.01 Hz, Figure 2a; Figure S10b in Supporting Information S1). To investigate this further, we analyzed real induction vectors (Parkinson convention). At frequencies greater than 1 Hz all induction vectors have small magnitudes, however at frequencies greater than 1 Hz there is no reliable tipper data available for the WAIS Divide stations (Figure S12 in Supporting Information S1). Given the near-identical XY and YX apparent resistivity depth profiles around the ice-bed interface (Figure S13 in Supporting Information S1), a 1-D modeling approach remains a robust and practical approximation for the shallow (near the ice-bed interface) structural interpretation.

At the TG stations upstream of GHOST Ridge, the apparent resistivity decreases significantly from 190 to 1 Hz (∼7,000 Ωm to ∼50 Ωm), consistent with a conductive subglacial sedimentary basin. However, at GHOST Ridge, in the absence of a known thick sedimentary basin (Borthwick et al., 2025; Jordan et al., 2023), the apparent resistivity remains higher (∼7,000 Ωm to ∼2,000 Ωm), Figure 2b. The phase tensors at the highest frequencies (190–10 Hz) generally plot as circles reflecting the 1-D nature of the subglacial resistivity structure (Figure 2a; Figure S10a in Supporting Information S1) consistent with the similarity of the XY and YX curves shown in Figure S13 of Supporting Information S1. As frequencies decrease into the 1–0.01 Hz band, sampling the deeper subglacial structure (>∼10 km), the XY and YX apparent resistivity values diverge (Figure 2b) indicating a transition into a 2-D or 3-D resistivity structure. To further characterize this subglacial complexity at TG, we examined the phase tensors and induction vectors. At frequencies below 1 Hz, the phase tensors plot as ellipses. At GHOST Ridge, the major axes are oriented North-South at all frequencies <1 Hz (Figure 2a; Figure S10a in Supporting Information S1). In contrast, the upstream stations show the major axes are oriented East-West at all frequencies less than 1 Hz (Figure 2a; Figure S10a in Supporting Information S1). Real induction vectors (Parkinson convention) provide evidence of 3-D structure (Figure S11 in Supporting Information S1) as the vectors exhibit systematic, frequency-dependent rotation. Specifically, at intermediate frequencies (1–0.1 Hz), vectors at the downstream sites TG7 and TG35 point generally southwest and rotate northwest at frequencies greater than 0.1 Hz (Figure 2a; Figure S11 in Supporting Information S1). The systematic rotation observed at the downstream sites precludes a 2-D interpretation. Because the induction vectors rotate with frequency and do not maintain a uniform alignment with the principal phase tensor axes, the deeper (>∼10 km depth) subglacial resistivity structure at TG is likely 3-D.

The Bayesian Z_{ssq} inversion of the WAIS Divide data is shown in Figures S15–S17 of Supporting Information S1 and exhibits high bulk resistivity, ranging from 450 to 1,400 Ωm, beneath the ice sheet extending to 1 km within the upper crust. This is consistent with the absence of a subglacial sedimentary basin. By contrast, low resistivities

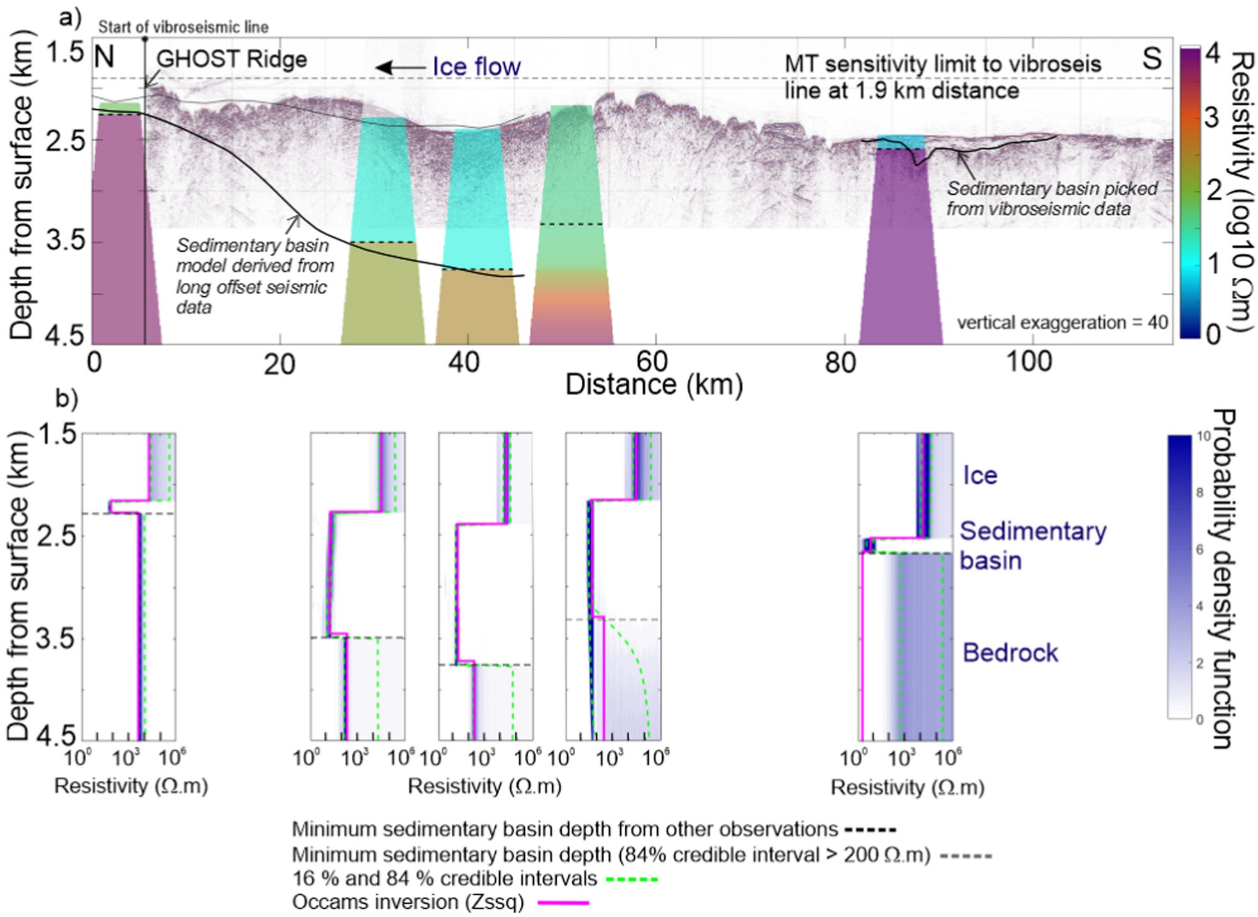

Figure 3. (a) Vibroseis line acquired along the MT profile (Zeising et al., 2026), 1.9 km East of the MT stations (Figure 2a), with the median resistivity from the 1-D Bayesian inversion of the Z_{ssq} data overlaid. Additionally, the sedimentary basin model derived from long offset seismic is plotted (Borthwick et al., 2025). The MT results are plotted as a cone shape representing the horizontal sensitivity of the data with depth from the surface of the ice sheet (Berdichevsky & Dmitriev, 2008). (b) Posterior distribution of resistivity with depth, output from the 1-D Bayesian inversion for the Z_{ssq} impedance tensors with the 1-D Occam's inversion results overlaid (magenta line). The 16% and 84% credible intervals (one standard deviation) are shown by the green dotted lines.

are observed beneath the base of the TG and are consistent with the presence of two distinct sedimentary basins (Figure 3; Figures S18–S20 in Supporting Information S1).

The first basin is located adjacent to and upstream of GHOST Ridge (Borthwick et al., 2025) and exhibits horizontal variations in resistivity. The most conductive part of this basin (~14 Ωm, with a 68% credible interval of 13–16 Ωm) corresponds to the location where the basin is thickest (~1,400 m) and where the vibroseis data (Zeising et al., 2026) show the smoothest bed topography (Figure 3). The thinnest part of the basin (~130 m) is on GHOST Ridge and has a higher resistivity (~73 Ωm, with a 68% credible interval of 62–88 Ωm). At this location the bed topography is relatively rough (Figure 3).

A second, thinner basin is also imaged with similar low resistivity values (~6 Ωm, with a 68% credible interval of 4–12 Ωm) and a thickness of approximately ~150 m, constrained by vibroseis data (Figure 3; Zeising et al., 2026). However, resistivity estimates for this second basin are less certain as significant noise contaminates the MT data at frequencies below 5 Hz. This was likely caused by electric field noise caused by wind-blown, statically charged ice particles in high wind speeds, during data acquisition (Figure S5 in Supporting Information S1). Therefore, we have excluded this station from our extended analysis in the Discussion section.

The resistivity-depth models obtained by inversion of the independent Z_{xy} and Z_{yx} data are very similar to the models derived from inversion of the Z_{ssq} data (within the 68% credible interval range) for the WAIS Divide and TG upper crustal structure discussed above (Figures S15–S20 in Supporting Information S1). This confirms the validity of our 1-D inversion approach at these shallow crustal depths. Furthermore, the results of the Occam's inversion agree well with the Bayesian inversion models (Figure 3b; Figures S15–S19 in Supporting Information S1). The only exception is the MT station (TG90) located 90 km along the vibroseis line, where poor data quality at mid to low frequencies, as discussed above, leads to divergence at depths below the imaged sedimentary basin (>2.6 km).

3.2. Compilation of Legacy West Antarctic and South Pole MT Data Sets

To place the new data in context, we also applied MuLTI-MT, with the same inversion parameters detailed in Table S1 of Supporting Information S1, to the inversion of the Z_{ssq} impedance data of legacy MT data acquired on the Whillans Ice Stream (Gustafson et al., 2022), Central West Antarctica (Wannamaker et al., 1996), South Pole (Wannamaker et al., 2004), and Ross Ice Shelf (Wannamaker et al., 2017).

The results from our 1-D Bayesian inversions are consistent with previously published 2-D and 3-D inversion models (Gustafson et al., 2022; Wannamaker et al., 2023) and, crucially, provide additional rigorous quantification of model uncertainty (Figures S21–S30 in Supporting Information S1). Subglacial resistivities (directly beneath the ice) are consistently low (<200 Ωm) where the presence of sedimentary basins are inferred, including TG, Whillans Ice Stream, the South Pole and Ross IS (Figure 4). In contrast, locations at WAIS Divide and Central West Antarctica show significantly more resistive subglacial material (>200 Ωm), consistent with the absence of a detectable layer of sedimentary rock (Figure 4).

Li and Aitken (2024) developed a continental-scale sedimentary basin model using seismic-constrained 3-D gravity inversion (Figure 4a). Here, we compare the minimum subglacial basin thickness estimated from the MT data with the continental-scale model and show kilometer-scale discrepancies in basin thicknesses at TG, along Whillans Ice Stream and at the South Pole, while showing closer agreement on the Ross Ice Shelf (Figure 4b). These differences demonstrate the potential for iteratively updating continental-scale models. By providing new, localized constraints from direct geophysical observations, our MT results offer potential tie-points that can be assimilated into future model iterations to help constrain regional variability and reduce spatial uncertainties.

The resistivity models derived from the MT data also highlight variability in resistivity among the basins (Figures 4c and 4d). The TG basin is characterized by a relatively high resistivity of 14–73 Ωm. The Whillans Ice Stream grounding zone has a narrow range of 7–8 Ωm, while the Ross IS is less resistive (2–5 Ωm). In the TG, WGZ and Ross IS basins, the posterior resistivity distributions are consistent with a vertically uniform resistivity structure, suggesting that any vertical variation in bulk resistivity is minor and falls below the sensitivity of the MT method (Figure 3b; Figures S23 and S27 in Supporting Information S1). In contrast, at SLW and South Pole, the posterior distribution with depth reveals a two-layer resistivity structure within these sedimentary basins (Figures S21 and S25 in Supporting Information S1). At SLW, this stratigraphy comprises of a low-resistivity thin upper layer (200–600 m thick; 4–10 Ωm; Figures 4c and 4d) overlying an even lower-resistivity lower layer (700–1,500 m thick; 2–5 Ωm; Figures 4c and 4d), consistent with the results of Gustafson et al. (2022). The four stations closest to the South Pole show a relatively resistive thin upper layer (200–500 m thick; 20–320 Ωm; Figures 4c and 4d) overlying a lower-resistivity lower layer (550–1100 m thick; 1–5 Ωm; Figures 4c and 4d), consistent with the 2-D model of Wannamaker et al. (2004) and the 3-D model reported in Wannamaker et al. (2023). The 3-D inversion of the South Pole data further characterized this feature as conductive layering directly below the ice sheet, noting its undulatory nature likely indicating marked lateral variations in its geometry or thickness.

As MT methods are sensitive to layer conductance, we additionally calculated the conductance of the subglacial sedimentary basins. This robust parameter clearly highlights the differences in bulk electrical properties between the basins (Figure 4e), confirming their heterogeneous nature. The resulting inferred variability in the electrical structure between all basins is large and provides critical new information for understanding their distinct geological, geothermal, and hydrogeological properties.

4. Discussion

4.1. Estimating Sedimentary Basin Properties and Pore Fluid Salinity

Spatial heterogeneity in the resistivity of the sedimentary basins in our study can be attributed to several factors, including differences in lithology, temperature and the concentration of solutes in subglacial groundwater. The sedimentary basins underlying TG, the South Pole region, the Whillans Ice Stream, and the Ross IS each have

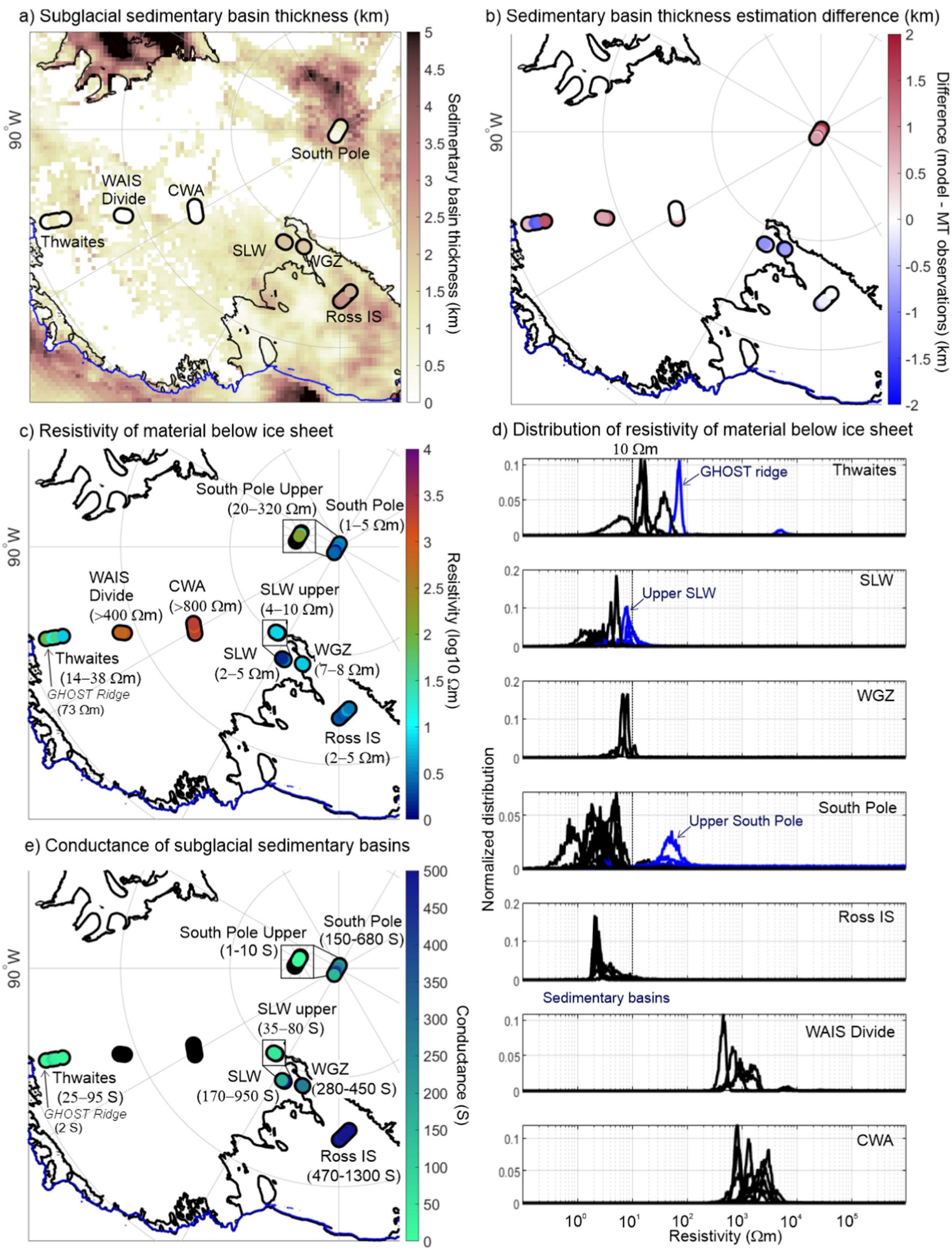

Figure 4. (a) Continent-scale sedimentary basin thickness model from Li and Aitken (2024), with the minimum sedimentary basin thickness derived from the MT. We note that the TG basin thickness is constrained by seismic observations as shown in Figure 3. (b) Difference between the sedimentary basin model of Li and Aitken (2024) and minimum thickness derived from MT. (c) Resistivity of the material below the ice sheet, the colormap applied follows that used in Gustafson et al. (2022) and Mikucki et al. (2015). (d) Histogram of resistivity of material below the ice sheet for all MT inversion outputs. (e) Conductance of subglacial sedimentary basins.

Table 1
Summary of Estimated Properties for the Studied Sedimentary Basins

Sedimentary basin	Basin bulk resistivity (Ωm) [14%, 86% credible interval]	Minimum basin thickness derived from MT (m)	GHF (mW/m^2)
GHOST Ridge	73 [62,88]	130 (constrained by seismic observations)	100–200
Thwaites	14-38 [13,49]	1200–1400 (constrained by seismic observations)	
Upper SLW	4–10 [4,16]	200–600	285 ± 80
SLW	2–5 [1,6]	1000–2000	
WGZ	7–8 [5,12]	2000–3000	88 ± 7
Upper South Pole	20–320 [5,70 000]	200–500	120 ± 20
South Pole	1–5 [0.5,18]	300–1400	
Ross IS	2–5 [2,14]	2300–3000	55

Note. GHF values are from Fisher et al. (2015) for SLW, Begeman et al. (2017) for WGZ, Jordan et al. (2018) for the South Pole, Schroder et al. (2014) for Thwaites, and Begeman et al. (2017) for the Ross Ice Shelf.

distinct origins and compositions, reflecting the varied geological history of West and East Antarctica (Figure 1c; Aitken et al., 2023).

Estimating the intrinsic properties and pore fluid salinity of the subglacial sedimentary basins from bulk resistivity alone presents a challenge due to non-uniqueness. For instance, a relatively high resistivity can be attributed to low porosity, low temperature, low salinity pore fluids, frozen or partially frozen pore fluids, trapped hydrocarbons, low clay content or a combination of all these factors. Conversely, relatively low resistivity can result from high porosity, high temperatures, elevated salinity, or high clay content (particularly smectite; Revil & Glover, 1998).

Given the inherent trade-offs between these parameters, we conducted two sensitivity tests to explore the coupled effects of key sedimentary basin parameters, porosity and temperature, on the estimated pore fluid salinity. We employed the empirical relationship of Archie's law (Equation S1 in Supporting Information S1; Archie, 1942) and the practical salinity scale of Lewis and Perkin (1981) for this analysis. Due to the high number of unknown parameters, these tests were designed to provide a range, rather than an explicit value, for the likely pore fluid salinity. Following this sensitivity study, we summarize all estimated properties in Table 1.

To examine the influence of porosity, a property potentially linked to variations in lithology and basin origin, we assumed a range of cementation exponents (m) appropriate for sedimentary rocks ($m = 1.5$ to 2.0; Archie, 1942). We kept temperature and pressure constant at 0°C and 1 bar, respectively, simulating conditions at/near the ice-bed interface. The porosity was varied from 0.01 to 0.65, consistent with the expected range for sedimentary rocks (Schön, 2015). Our results reveal a potential difference in the estimated pore fluid salinity between the GHOST Ridge, upper SLW and upper South Pole sediments from their more conductive lower units, within the sedimentary basins (Figures 5a, 5b, and 5d). Consequently, at TG, variations in porosity alone could account for the observed resistivity contrast between the GHOST Ridge sediments and the less resistive, thicker part of the TG basin. For instance, a mid-porosity unit ($\phi \approx 0.2$) could yield the higher bulk resistivity observed at GHOST Ridge, while a high-porosity unit ($\phi \approx 0.3$–0.6) could explain the lower resistivity of the basin, even if both were saturated with identical brackish, 2 Practical Salinity Units (PSU), pore fluids (Figure 5a). However, at South Pole basin, the relatively resistive upper layer identified in the four stations closest to the South Pole, termed Upper South Pole, shows a distinct separation of pore fluid salinity at all porosities, suggesting a change in pore fluid could fit the observed MT data.

We also investigated the influence of temperature, a property directly linked to GHF, on pore fluid salinity. Temperature gradients are derived from GHF using Fourier's law of heat conduction. However, it is important to note that calculating absolute temperatures from surface heat flux carries significant uncertainty, as it relies on site-specific thermal conductivity values which, unless directly measured, must be estimated from assumed basin characteristics. For this sensitivity test, we kept porosity constant at 0.2 and pressure at 1 bar. We again used a range of Archie's exponents (m) from 1.5 to 2.0. We modeled temperatures ranging from 0°C to 250°C to consider the plausible and extreme thermal conditions within the basin. The lower bound (0°C) represents the ice-bed interface, while the upper bound (250°C) corresponds to the projected temperature at a depth of 1 km, chosen

10.1029/2026JB033859

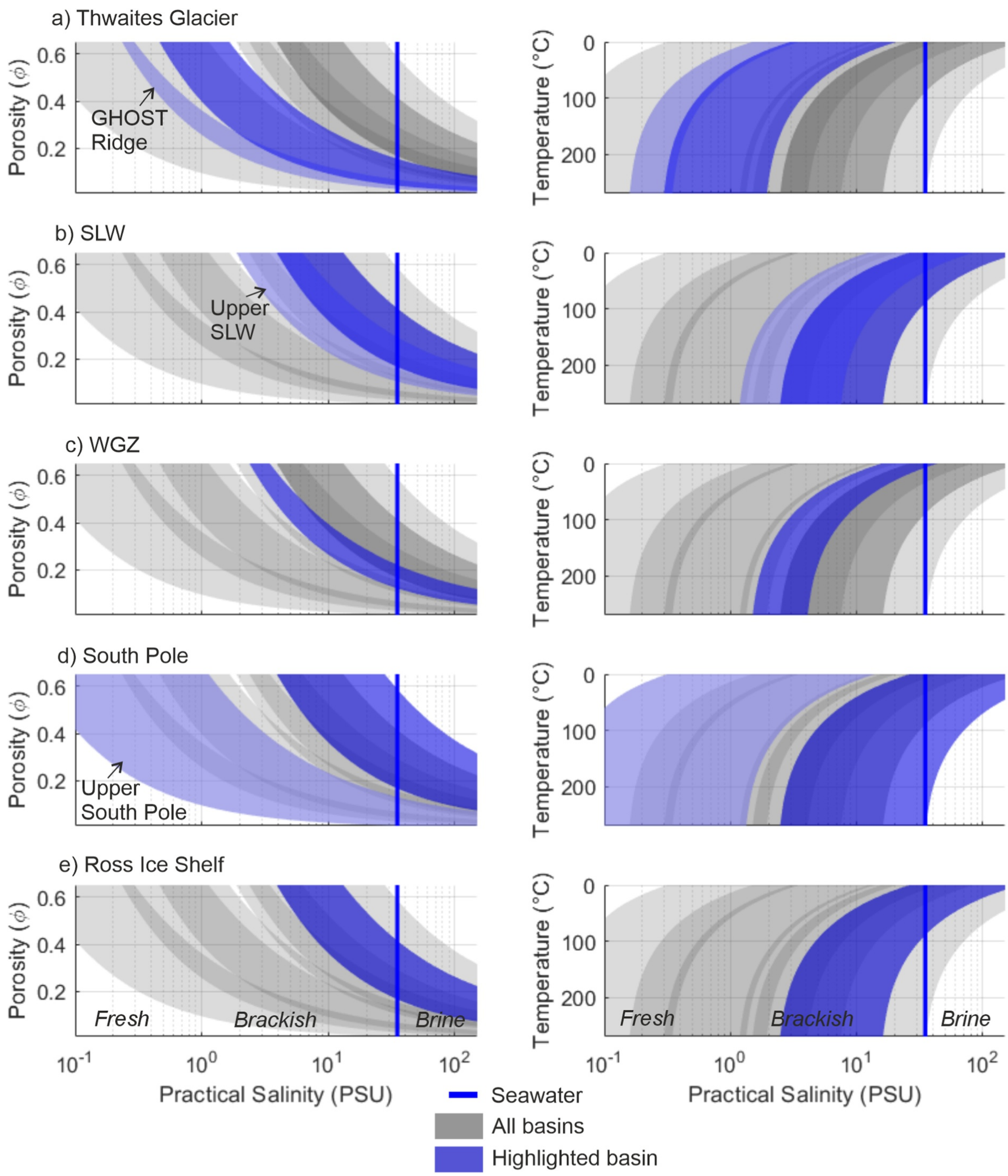

Figure 5. Left: Pore fluid practical salinity versus porosity for each sedimentary basin calculated using the average bulk resistivity shown in Figure 4c and Archie's Law (with m = 1.5–2.0, temperature = 0°C and pressure = 1 bar). Right: Pore fluid practical salinity versus temperature for each sedimentary basin calculated using the average bulk resistivity shown in Figure 4c and Archie's Law (with m = 1.5–2.0, porosity = 0.2 and pressure = 1 bar).

as a representative depth within the sedimentary column, assuming the extreme GHF and thermal conductivity gradients observed at SLW (Begeman et al., 2017). Our results show a substantial decrease in the estimated pore fluid salinity with increasing temperature (Figure 5). Furthermore, at temperatures exceeding 90°C, the salinity of the pore fluid for all basins modeled becomes less than that of seawater (Figure 5). Therefore, strong temperature gradients could be the cause of variable sedimentary basin resistivities. Again, at South Pole basin and the four stations where the Upper South Pole layer exists, there is a constant separation of pore fluid salinity from the more conductive deeper basin, at all temperatures modeled.

A key caveat to these interpretations is the potential influence of conductive clay minerals, which are not accounted for in Archie's Law (Kulessa et al., 2006; Revil & Cathles, 1999). A quantitative analysis of clay content is beyond the scope of this study due to numerous unknown parameters. However, a qualitative assessment based on regional geology is possible. In the Amundsen Sea, which is the drainage region for TG, clay mineral assemblages are dominated by kaolinite (Hillenbrand et al., 2003). While the region can be broadly defined as a "kaolinite province" (Hillenbrand et al., 2003), a clay mineral with a simple crystal structure that has a minimal effect on bulk resistivity (Revil & Glover, 1998), the smectite content is unknown. Smectite has a high cation exchange capacity that significantly lowers bulk resistivity (Revil & Glover, 1998). In this region, smectite could be derived from the weathering of volcanic rocks in the hinterland (Herbert et al., 2023). Thus, erosion from Mt. Takahe or Mt. Murphy could supply conductive clays to the TG basin, contributing to the observed low resistivity. This is also the case for the Eastern Ross Sea, where sediments sourced from the WARS may have a high smectite content. The coastal sedimentary basins beneath the Whillans Ice Stream contains marine clays (Hodson et al., 2016) which will also have a non-negligible effect on the resistivity of these basins (Aitken et al., 2023).

4.2. New Insights Into West Antarctic Crustal Framework

The combined analysis of phase tensors and real induction vectors at TG shows the data are consistent with a shallow (<~5 km) 1-D structure and a deeper (>~10 km) 3-D structure. The frequency-dependent rotation of the induction vectors, pointing southwest at higher frequencies (~0.2 Hz) and northwest at lower frequencies (~0.1 Hz), implies a depth-dependent geometry (Figure 2a). This suggests the conductive source extends deeper in the northwest and shallows toward the southwest. The source of the shallow southwest conductor could be the western end of the TG sedimentary basin, as discussed earlier in Section 3.1. However, crucially, Jordan et al. (2023) and Borthwick et al. (2025) inferred that no sedimentary basins were present in the region northwest of GHOST Ridge, suggesting the deeper conductive zone is located in the basement rocks rather than the overlying sedimentary layers.

While the dominant shallow East-West structure appears to be controlled by the Cretaceous West Antarctic Rift System (WARS), the deeper architecture may be influenced by an older tectonic framework. Jordan et al. (2023) identified highly magnetic (>200 nT) Northwest-Southeast aligned structures, interpreting them as either: (a) magnetic West Antarctic basement predating the WARS, or (b) subglacial intrusions associated with Cenozoic volcanism (Figure 2a). The latter is plausible given the proximity to shield volcanoes such as Mt. Takahe; however, the orientation aligns with older tectonic trends. Aitken et al. (2023) identified structures related to the Jurassic Weddell Sea Rift System (WSRS) extending into the Amundsen Sea Sector and the TG area (Figure 1c). Therefore, while the shallower resistivity structure is defined by WARS extension, the deeper 3-D conductor could be controlled by structural inheritance from the older WSRS, which may act as a preferred pathway for fluids, or Cenozoic volcanism.

Beyond the structural controls of the upper crust, the deep electrical resistivity structure provides critical constraints on the thermal state and hydration of the underlying lithosphere, key boundary conditions for GHF and ice dynamics models (Reading et al., 2022). Deep crustal and upper mantle resistivity is highly sensitive to temperature, which enhances ionic mobility, and the presence of fluids or partial melt (e.g., Samrock et al., 2015). A recent re-analysis of Antarctic MT data by Wannamaker et al. (2023) established three regional end-members: (a) CWA, characterized by high resistivity (>500 Ωm) indicative of a cold, near-cratonic lithosphere; (b) the South Pole, exhibiting low resistivity (<10 Ωm) consistent with an elevated thermal regime and high GHF (~120 mW/m^2; Jordan et al., 2018); and (c) the Ross IS, representing an intermediate state where resistivity is controlled by moderate mantle hydration, but not sufficient to induce melting.

Our 1-D Bayesian inversions for TG and WAIS Divide reveal bulk resistivities in the 30–40 km depth interval, interpreted as upper mantle (Dunham et al., 2020), ranging from ~200 to 300 Ωm at WAIS Divide and ~40–400 Ωm at TG (Figures S12 and S15 in Supporting Information S1). Notably, these values are more conducive than the cold lithosphere of CWA but do not reach the extreme conductivity associated with the high thermal anomaly at the South Pole. Instead, the upper bounds of our resistivity estimates are comparable to the ~300 Ωm values reported for the Ross IS region (Wannamaker et al., 2023). This suggests that the upper mantle beneath TG and WAIS Divide may exist in a similar state to that of the Ross IS, generally cooler than the South Pole basin, but with resistivity reduced by moderate hydration. However, given the inherent non-uniqueness of 1-D inversions in a 3-D environment, these hypotheses regarding framework, deep hydration and thermal state warrants further testing through dedicated 3-D modeling.

4.3. MT Data Constraints and Future Perspectives in West Antarctica

Acquiring MT data in deep-field Antarctic environments, such as TG which is one of the most remote locations on Earth, presents unique logistical and environmental challenges that fundamentally influence survey design and data processing. Unlike terrestrial surveys (deployed on land) where dense, 3-D arrays with hundreds of stations are standard, deep-field deployments on ice sheets are heavily constrained by limited personnel, extreme weather, and strict operational timeframes. Consequently, MT acquisition can be limited to sequential, single-station deployments. This results in several issues that impact data quality.

The data presented here exhibit degraded quality in the deadband (∼1–10 Hz), which is exacerbated by high wind conditions and electrostatically charged blowing snow. Standard terrestrial processing often relies on a distant remote reference station to mitigate such noise. Given the logistical constraints of deep-field deployments, establishing a distant, quiet site to escape coherent wind and ionospheric noise is rarely feasible. While cross-referencing within a local, simultaneously recording array is a practical alternative, it remains vulnerable to regional weather. When high winds occur, mechanical vibrations and electrostatic discharge can affect all local stations simultaneously, creating correlated noise that effectively neutralizes the mathematical benefits of cross-referencing algorithms. To overcome this limitation, we employed a time-based pre-filtering approach. High-amplitude noise bursts associated with storms, strong wind events, were identified in the time series and selectively excluded using the EMpower Time Editor (Phoenix Geophysics). This manual pre-filtering supplemented the software's standard robust estimation algorithms, ensuring that only clean, calm data windows were utilized for processing and preventing coherent wind artifacts from biasing the final MT response.

Furthermore, future campaigns can mitigate the observed loss of high-frequency data (>200 Hz) by systematically measuring the contact resistance at each site using an analog multimeter, allowing for the mathematical deconvolution of the system's transfer function, specifically the interaction between high contact resistance and instrumental input capacitance, during processing.

Despite the absence of remote referencing and the loss of high-frequency data (>200 Hz), robust modeling of the data to produce a resistivity model is still achievable. By incorporating high-resolution ice thickness observations to fix the depth of the highly resistive ice layer, the inversion can reliably resolve the conductance of the underlying subglacial material. Furthermore, incorporating seismic observations, such as the sedimentary basin thickness utilized in this study, significantly reduces the non-uniqueness inherent to MT inversions.

To further refine interpretations of subglacial resistivity structures, future studies could aim to integrate additional independent constraints such as seismic velocity models. This could provide robust estimates of basin porosity, helping to isolate the effect of pore-fluid salinity on bulk resistivity.

The identification of a deeper, potentially 3-D conductive structure near TG warrants further investigation. Future MT surveys should target the region west and northwest of GHOST Ridge to delineate this deep conductor and investigate its potential association with Cenozoic volcanism (e.g., Mt. Takahe and Mt. Murphy) or structural inheritance from the older WSRS. Prior to deployment, 3-D forward modeling based on our current 1-D profiles and existing aeromagnetic structures could be utilized to optimize station spacing and survey design. With national equipment pools making more MT systems available, there is significant potential to expand MT coverage. These future surveys will be critical for imaging the subglacial hydrological environments that directly control ice dynamics, as well as the deep crustal and upper mantle architectures that dictate geothermal heat flux across the continent.

5. Conclusions

By combining new and legacy MT data, we identify a potential contrast between the relatively high resistivity basin beneath TG (>10 Ωm) and the low resistivity basins that characterize the Whillans Ice Stream, Ross Ice Shelf, and South Pole regions (<10 Ωm). This distinction points to differing geological histories and associated hydrogeological and geothermal processes, with varying groundwater regimes likely widespread in West Antarctic sedimentary basins.

The horizontal resistivity variations observed across the TG basin indicate that the basin may be horizontally heterogeneous. In contrast, the models for SLW and the South Pole reveal a two-layer vertical resistivity structure. In these basins, the upper layer at the ice-bed interface is more resistive, similar to the resistivity estimated at GHOST Ridge, while the deeper basin is more conductive. These inter-basin heterogeneities highlight the potential for complex, distinct groundwater regimes across Antarctica, with consequent variable impacts on groundwater advection, basal melting, and the exchange of fluids between the ice-bed interface and deeper hydrological systems.

This research demonstrates the utility of the MT method for characterizing subglacial sedimentary basins and underscores the critical role of constraining parameters such as porosity, temperature, and clay mineralogy, which remain primary sources of uncertainty. The discrepancies identified between our localized basin thickness estimates and continent-scale models highlight the value of integrating direct geophysical constraints into the next generation of continental sedimentary basin models. These advances will facilitate a robust understanding of how deep groundwater and geothermal heat interact with the subglacial interface.

Conflict of Interest

The authors declare no conflicts of interest relevant to this study.

Availability Statement

MuLTI MT is available from Killingbeck (2025). The Thwaites Glacier magnetotellurics data are available from Brisbourne et al. (2026). The WAIS Divide magnetotellurics data are available from Pearce et al. (2026).

Acknowledgments

This work was supported by NERC under Grant NE/S006672/1 and NSF under Grants PLR-1738934, OPP-2001714, and OPP-2002346. The magnetotelluric equipment was supplied by NERC Geophysical Equipment Facility under loan 1125. We thank all members of the GHOST field teams, British Antarctic Survey Operations and US Antarctic Program staff at WAIS Divide for facilitating and assisting in the collection of the data. Special thanks to the BAS Traverse Leader Catrin Thomas as well as field guide and "MT expert" Mark Chambers. We also thank Chloe Gustafson for her expert advice and useful discussions on this research. This work is from the Geophysical Habitat of Subglacial Thwaites (GHOST) project, a component of the International Thwaites Glacier Collaboration (ITGC). Additional members of the ITGC GHOST team are Ronan Agnew, Richard Alley, Rob Arthern, Robert Bingham, Julien Bodart, Elizabeth Case, Knut Christianson, Olaf Eisen, Kevin Hank, Andrew Hoffman, Coen Hofstede, Nick Holschuh, Jonny Kingslake, Sierra Melton, Helen Ockenden, Byron R. Parizek, Kiya Riverman, Emily Schwans, Andy Smith, Leigh Stearns, Nathan Stevens, Paul Winberry, Amanda Willet, Jaiden Zak, Ole Zeising, and Luke Zoet. ITGC contribution No. ITGC-152.

References

Aitken, A. R., Li, L., Kulessa, B., Schroeder, D., Jordan, T. A., Whittaker, J. M., et al. (2023). Antarctic sedimentary basins and their influence on ice-sheet dynamics. *Reviews of Geophysics*, *61*(3), e2021RG000767. https://doi.org/10.1029/2021RG000767

Alley, R. B., Anandakrishnan, S., Bentley, C. R., & Lord, N. (1994). A water-piracy hypothesis for the stagnation of Ice Stream C, Antarctica. *Annals of Glaciology*, *20*, 187–194. https://doi.org/10.3189/1994AoG20-1-187-194

Alley, R. B., Blankenship, D. D., Bentley, C. R., & Rooney, S. T. (1987). Till beneath ice stream B: 3. Till deformation: Evidence and implications. *Journal of Geophysical Research*, *92*(B9), 8921–8929. https://doi.org/10.1029/JB092iB09p08921

Anandakrishnan, S., Blankenship, D. D., Alley, R. B., & Stoffa, P. L. (1998). Influence of subglacial geology on the position of a west Antarctic ice stream from seismic observations. *Nature*, *394*(6688), 62–65. https://doi.org/10.1038/27889

Archie, G. E. (1942). The electrical resistivity log as an aid in determining some reservoir characteristics. *Transactions of the AIME*, *146*(1), 54–62. https://doi.org/10.2118/942054-g

Begeman, C. B., Tulaczyk, S. M., & Fisher, A. T. (2017). Spatially variable geothermal heat flux in west Antarctica: Evidence and implications. *Geophysical Research Letters*, *44*(19), 9823–9832. https://doi.org/10.1002/2017GL075579

Bell, R. E., Blankenship, D. D., Finn, C. A., Morse, D. L., Scambos, T. A., Brozena, J. M., & Hodge, S. M. (1998). Influence of subglacial geology on the onset of a west Antarctic ice stream from aerogeophysical observations. *Nature*, *394*(6688), 58–62. https://doi.org/10.1038/27883

Berdichevsky, M. N., & Dmitriev, V. I. (2008). *Models and methods of magnetotellurics*. Springer Science & Business Media.

Bingham, R. G., Ferraccioli, F., King, E. C., Larter, R. D., Pritchard, H. D., Smith, A. M., & Vaughan, D. G. (2012). Inland thinning of west Antarctic ice sheet steered along subglacial rifts. *Nature*, *487*(7408), 468–471. https://doi.org/10.1038/nature11292

Borthwick, L., Muto, A., Anandakrishnan, S., Tinto, K., Agnew, R., Brisbourne, A., et al. (2025). Rift-related sedimentary basin and deeper-seated mafic intrusions modeled beneath Thwaites Glacier, west Antarctica: Influence on glacier dynamics. *Journal of Geophysical Research: Solid Earth*, *130*(10), e2025JB031716. https://doi.org/10.1029/2025JB031716

Brisbourne, A., Borthwick, L., Napoleoni, F., Anandakrishnan, S., Kulessa, B., & Killingbeck, S. (2026). Magnetotelluric survey from Thwaites Glacier, December 2023 to January 2024 (version 1.0) [Dataset]. *NERC EDS UK Polar Data Centre*. https://doi.org/10.5285/88187258-C49F-4897-B158-5A13258566AF

Caldwell, T. G., Bibby, H. M., & Brown, C. (2004). The magnetotelluric phase tensor. *Geophysical Journal International*, *158*(2), 457–469. https://doi.org/10.1111/j.1365-246X.2004.02281.x

Chave, A. D. & Jones, A. G. (Eds.) (2012)., *The magnetotelluric method: Theory and practice*. Cambridge University Press.

Clyne, E. R., Anandakrishnan, S., Muto, A., Alley, R. B., & Voigt, D. E. (2020). Interpretation of topography and bed properties beneath Thwaites Glacier, west Antarctica using seismic reflection methods. *Earth and Planetary Science Letters*, *550*, 116543. https://doi.org/10.1016/j.epsl.2020.116543

Constable, S. C., Parker, R. L., & Constable, C. G. (1987). Occam's inversion: A practical algorithm for generating smooth models from electromagnetic sounding data. *Geophysics*, *52*(3), 289–300. https://doi.org/10.1190/1.1442303

Cox, S. C., Smith Lyttle, B., Elkind, S., Smith Siddoway, C., Morin, P., Capponi, G., et al. (2023). A continent-wide detailed geological map dataset of Antarctica. *Scientific Data*, *10*(1), 250. https://doi.org/10.1038/s41597-023-02152-9

Dunham, C. K., O'Donnell, J. P., Stuart, G. W., Brisbourne, A. M., Rost, S., Jordan, T. A., et al. (2020). A joint inversion of receiver function and rayleigh wave phase velocity dispersion data to estimate crustal structure in west Antarctica. *Geophysical Journal International*, *223*(3), 1644–1657. https://doi.org/10.1093/gji/ggaa398

Fisher, A. T., Mankoff, K. D., Tulaczyk, S. M., Tyler, S. W., & Foley, N., & WISSARD Science Team. (2015). High geothermal heat flux measured below the west Antarctic Ice Sheet. *Science Advances*, *1*(6), e1500093. https://doi.org/10.1126/sciadv.1500093

García, K., & Díaz, D. (2016). Three-dimensional geo-electrical structure in juncalito geothermal prospect, northern Chile. *Geothermics*, *64*, 527–537. https://doi.org/10.1016/j.geothermics.2016.08.001

Gooch, B. T., Young, D. A., & Blankenship, D. D. (2016). Potential groundwater and heterogeneous heat source contributions to ice sheet dynamics in critical submarine basins of East Antarctica. *Geochemistry, Geophysics, Geosystems*, *17*(2), 395–409. https://doi.org/10.1002/2015GC006117

Greene, C. A., Gwyther, D. E., & Blankenship, D. D. (2017). Antarctic mapping tools for MATLAB. *Computers & Geosciences*, *104*, 151–157. https://doi.org/10.1016/j.cageo.2016.08.003

Gustafson, C. D., Key, K., Siegfried, M. R., Winberry, J. P., Fricker, H. A., Venturelli, R. A., & Michaud, A. B. (2022). A dynamic saline groundwater system mapped beneath an Antarctic ice stream. *Science*, *376*(6593), 640–644. https://doi.org/10.1126/science.abm3301

Herbert, L. C., Lepp, A. P., Garcia, S. M., Browning, A., Miller, L. E., Wellner, J., et al. (2023). Volcanogenic fluxes of iron from the seafloor in the Amundsen Sea, west Antarctica. *Marine Chemistry*, *253*, 104250. https://doi.org/10.1016/j.marchem.2023.104250

Hill, G. J. (2020). On the use of electromagnetics for earth imaging of the polar regions. *Surveys in Geophysics*, *41*(1), 5–45. https://doi.org/10.1007/s10712-019-09570-8

Hillenbrand, C. D., Grobe, H., Diekmann, B., Kuhn, G., & Fütterer, D. K. (2003). Distribution of clay minerals and proxies for productivity in surface sediments of the Bellingshausen and Amundsen seas (west Antarctica)–Relation to modern environmental conditions. *Marine Geology*, *193*(3–4), 253–271. https://doi.org/10.1016/S0025-3227(02)00659-X

Hodson, T. O., Powell, R. D., Brachfeld, S. A., Tulaczyk, S., & Scherer, R. P., & WISSARD Science Team. (2016). Physical processes in subglacial Lake Whillans, West Antarctica: Inferences from sediment cores. *Earth and Planetary Science Letters*, *444*, 56–63. https://doi.org/10.1016/j.epsl.2016.03.036

Jordan, T. A., Riley, T. R., & Siddoway, C. S. (2020). The geological history and evolution of west Antarctica. *Nature Reviews Earth & Environment*, *1*(2), 117–133. https://doi.org/10.1038/s43017-019-0013-6

Jordan, T. A., Martin, C., Ferraccioli, F., Matsuoka, K., Corr, H., Forsberg, R., et al. (2018). Anomalously high geothermal flux near the South Pole. *Scientific Reports*, *8*(1), 16785. https://doi.org/10.1038/s41598-018-35182-0

Jordan, T. A., Thompson, S., Kulessa, B., & Ferraccioli, F. (2023). Geological sketch map and implications for ice flow of Thwaites Glacier, west Antarctica, from integrated aerogeophysical observations. *Science Advances*, *9*(22), eadf2639. https://doi.org/10.1126/sciadv.adf2639

Key, K., & Siegfried, M. R. (2017). The feasibility of imaging subglacial hydrology beneath ice streams with ground-based electromagnetics. *Journal of Glaciology*, *63*(241), 755–771. https://doi.org/10.1017/jog.2017.36

Killingbeck, S. F. (2025). MuLTI MT. *Zenodo*. https://doi.org/10.5281/zenodo.17896670

Killingbeck, S. F., Dow, C. F., & Unsworth, M. J. (2022). A quantitative method for deriving salinity of subglacial water using ground-based transient electromagnetics. *Journal of Glaciology*, *68*(268), 319–336. https://doi.org/10.1017/jog.2021.94

Killingbeck, S. F., Rutishauser, A., Unsworth, M. J., Dubnick, A., Criscitiello, A. S., Killingbeck, J., et al. (2024). Misidentified subglacial lake beneath the Devon ice cap, Canadian Arctic: A new interpretation from seismic and electromagnetic data. *The Cryosphere*, *18*(8), 3699–3722. https://doi.org/10.5194/tc-18-3699-2024

Kulessa, B. (2007). A critical review of the low-frequency electrical properties of ice sheets and glaciers. *Journal of Environmental & Engineering Geophysics*, *12*(1), 23–36. https://doi.org/10.2113/JEEG12.1.23

Kulessa, B., Hubbard, B., & Brown, G. H. (2006). Time-lapse imaging of subglacial drainage conditions using three-dimensional inversion of borehole electrical resistivity data. *Journal of Glaciology*, *52*(176), 49–57. https://doi.org/10.3189/172756506781828854

Kulessa, B., Key, K., Thompson, S., & Siegert, M. (2019). Heat and groundwater transport between the Antarctic ice sheet and subglacial sedimentary basins from electromagnetic geophysical measurements. In *SEG international exposition and annual meeting*. SEG. https://doi.org/10.1190/segam2019-3215566.1.D033S046R005.

Lewis, E. L., & Perkin, R. G. (1981). The practical salinity scale 1978: Conversion of existing data. *Deep-Sea Research, Part A: Oceanographic Research Papers*, *28*(4), 307–328. https://doi.org/10.1016/0198-0149(81)90002-9

Li, L., & Aitken, A. R. A. (2024). Crustal heterogeneity of Antarctica signals spatially variable radiogenic heat production. *Geophysical Research Letters*, *51*(2), e2023GL106201. https://doi.org/10.1029/2023GL106201

Li, L., Aitken, A. R. A., Lindsay, M. D., & Kulessa, B. (2022). Sedimentary basins reduce stability of Antarctic ice streams through groundwater feedbacks. *Nature Geoscience*, *15*(8), 645–650. https://doi.org/10.1038/s41561-022-00992-5

Mikucki, J. A., Auken, E., Tulaczyk, S., Virginia, R. A., Schamper, C., Sørensen, K. I., et al. (2015). Deep groundwater and potential subsurface habitats beneath an Antarctic dry valley. *Nature Communications*, *6*(1), 6831. https://doi.org/10.1038/ncomms7831

Morlighem, M., Rignot, E., Binder, T., Blankenship, D., Drews, R., Eagles, G., et al. (2020). Deep glacial troughs and stabilizing ridges unveiled beneath the margins of the Antarctic ice sheet. *Nature Geoscience*, *13*(2), 132–137. https://doi.org/10.1038/s41561-019-0510-8

Mouginot, J., Rignot, E., & Scheuchl, B. (2014). Sustained increase in ice discharge from the Amundsen Sea Embayment, west Antarctica, from 1973 to 2013. *Geophysical Research Letters*, *41*(5), 1576–1584. https://doi.org/10.1002/2013GL059069

Mouginot, J., Rignot, E., & Scheuchl, B. (2019). Continent-wide, interferometric SAR phase, mapping of Antarctic ice velocity. *Geophysical Research Letters*, *46*(16), 9710–9718. https://doi.org/10.1029/2019GL083826

Muto, A., Anandakrishnan, S., Alley, R. B., Horgan, H. J., Parizek, B. R., Koellner, S., et al. (2019). Relating bed character and subglacial morphology using seismic data from Thwaites Glacier, west Antarctica. *Earth and Planetary Science Letters*, *507*, 199–206. https://doi.org/10.1016/j.epsl.2018.12.008

Napoleoni, F., Jamieson, S. S., Ross, N., Bentley, M. J., Rivera, A., Smith, A. M., et al. (2020). Subglacial lakes and hydrology across the Ellsworth subglacial highlands, west Antarctica. *The Cryosphere*, *14*(12), 4507–4524. https://doi.org/10.5194/tc-14-4507-2020

Parkinson, W. D. (1959). Directions of rapid geomagnetic fluctuations. *Geophysical Journal International*, *2*(1), 1–14. https://doi.org/10.1111/j.1365-246x.1959.tb05776.x

Pearce, R., Borthwick, L., Anandakrishnan, S., Kulessa, B., Killingbeck, S., & Brisbourne, A. (2026). Magnetotelluric survey from the west Antarctic ice sheet (WAIS) Divide, December 2022 to January 2023 (version 1.0) [Dataset]. *NERC EDS UK Polar Data Centre*. https://doi.org/10.5285/E655503E-AC7B-429E-A4CF-BB32838E28BC

Peters, L. E., Anandakrishnan, S., Alley, R. B., Winberry, J. P., Voigt, D. E., Smith, A. M., & Morse, D. L. (2006). Subglacial sediments as a control on the onset and location of two siple Coast ice streams, west Antarctica. *Journal of Geophysical Research*, *111*(B1). https://doi.org/10.1029/2005JB003766

Reading, A. M., Stål, T., Halpin, J. A., Lösing, M., Ebbing, J., Shen, W., et al. (2022). Antarctic geothermal heat flow and its implications for tectonics and ice sheets. *Nature Reviews Earth & Environment*, *3*(12), 814–831. https://doi.org/10.1038/s43017-022-00348-y

Revil, A., & Cathles, L. M. (1999). Permeability of shaly sands. *Water Resources Research*, *35*(3), 651–662. https://doi.org/10.1029/98WR02700

Revil, A., & Glover, P. W. J. (1998). Nature of surface electrical conductivity in natural sands, sandstones, and shales. *Geophysical Research Letters*, *25*(5), 691–694. https://doi.org/10.1029/98GL00296

Rung-Arunwan, T., Siripunvaraporn, W., & Utada, H. (2017). Use of ssq rotational invariant of magnetotelluric impedances for estimating informative properties for galvanic distortion. *Earth Planets and Space*, *69*(1), 80. https://doi.org/10.1186/s40623-017-0665-8

Samrock, F., Kuvshinov, A., Bakker, J., Jackson, A., & Fisseha, S. (2015). 3-D analysis and interpretation of magnetotelluric data from the aluto-langano geothermal field, Ethiopia. *Geophysical Journal International*, *202*(3), 1923–1948. https://doi.org/10.1093/gji/ggv270

Scambos, T. A., Bell, R. E., Alley, R. B., Anandakrishnan, S., Bromwich, D. H., Brunt, K., et al. (2017). How much, how fast? A science review and outlook for research on the instability of Antarctica's Thwaites Glacier in the 21st century. *Global and Planetary Change*, *153*, 16–34. https://doi.org/10.1016/j.gloplacha.2017.04.008

Schmucker, U. (1970). Anomalies of geomagnetic variations in the southwestern United States. *Bulletin of the Scripps Institution of Oceanography of the University of California*.

Schön, J. H. (2015). *Physical properties of rocks: Fundamentals and principles of petrophysics*. Elsevier.

Schoof, C. (2012). Marine ice sheet stability. *Journal of Fluid Mechanics*, *698*, 62–72. https://doi.org/10.1017/jfm.2012.43

Schroeder, D. M., Blankenship, D. D., Young, D. A., & Quartini, E. (2014). Evidence for elevated and spatially variable geothermal flux beneath the west Antarctic ice sheet. *Proceedings of the National Academy of Sciences*, *111*(25), 9070–9072. https://doi.org/10.1073/pnas.1405184111

Schwans, E. (2026). *The role of bed rheology and topography in retreat of Thwaites Glacier: Model-driven perspectives on bed control and glacier stability* [Doctoral dissertation]. The Pennsylvania State University. Penn State Electronic Theses and Dissertations for Graduate School. Retrieved from https://etda.libraries.psu.edu/catalog/29881eps5217

Schwans, E., Parizek, B. R., Alley, R. B., Anandakrishnan, S., & Morlighem, M. M. (2023). Model insights into bed control on retreat of Thwaites Glacier, west Antarctica. *Journal of Glaciology*, *69*(277), 1241–1259. https://doi.org/10.1017/jog.2023.13

Siegert, M. J., Kulessa, B., Bougamont, M., Christoffersen, P., Key, K., Andersen, K. R., et al. (2018). Antarctic subglacial groundwater: A concept paper on its measurement and potential influence on ice flow. *Geological Society, London, Special Publications*, *461*(1), 197–213. https://doi.org/10.1144/SP461.8

Telford, W. M., Geldart, L. P., & Sheriff, R. E. (1990). *Applied geophysics*. Cambridge University Press.

Unsworth, M. J., & Rondenay, S. (2013). Mapping the distribution of fluids in the crust and lithospheric mantle utilizing geophysical methods. In D. E. Harlov & H. Austrheim (Eds.), *Chapter 13 in metasomatism and metamorphism: The role of fluids in crustal and upper mantle processes* (pp. 535–598). Springer-Verlag Berlin Heidelberg, Lectures in Earth Sciences. https://doi.org/10.1007/978-3-642-28394-9_13

Wannamaker, P., Hill, G., Stodt, J., Maris, V., Ogawa, Y., Selway, K., et al. (2017). Uplift of the central transantarctic mountains. *Nature Communications*, *8*(1), 1588. https://doi.org/10.1038/s41467-017-01577-2

Wannamaker, P. E., Stodt, J. A., & Olsen, S. L. (1996). Dormant state of rifting below the Byrd Subglacial Basin, west Antarctica, implied by magnetotelluric (MT) profiling. *Geophysical Research Letters*, *23*(21), 2983–2986. https://doi.org/10.1029/96GL02887

Wannamaker, P. E., Stodt, J. A., Hill, G. J., Maris, V., & Kordy, M. A. (2023). Thermal regime and state of hydration of the Antarctic upper mantle from regional-scale electrical properties. *Geological Society, London, Memoirs*, *56*(1), 181–194. https://doi.org/10.1144/M56-2020-4

Wannamaker, P. E., Stodt, J. A., Pellerin, L., Olsen, S. L., & Hall, D. B. (2004). Structure and thermal regime beneath the South Pole region, East Antarctica, from magnetotelluric measurements. *Geophysical Journal International*, *157*(1), 36–54. https://doi.org/10.1111/j.1365-246X.2004.02156.x

Weertman, J. (1974). Stability of the junction of an ice sheet and an ice shelf. *Journal of Glaciology*, *13*(67), 3–11. https://doi.org/10.3189/S0022143000023327

Weidelt, P. (1972). The inverse problem of geomagnetic induction. *Zeitschrift für Geophysik*, *38*, 257–289.

Zeising, O., Eisen, O., Hofstede, C., Agnew, R., Brisbourne, A., Hoffman, A. O., et al. (2026). Hard rocks and deep wetlands beneath Thwaites Glacier in Antarctica. *Communications Earth & Environment*, *7*(1), 366. https://doi.org/10.1038/s43247-026-03502-2